RESULTS FROM SUPER-KAMIOKANDE

Masayuki NAKAHATA
Kamioka Observatory, Institute for Cosmic Ray Research
University of Tokyo, Higashi-Mozumi, Kamioka-cho, Yoshiki-gun
Gifu, Japan, 506-1205

For the Super-Kamiokande Collaboration

ABSTRACT

The results from Super-Kamiokande on atmospheric neutrinos and solar neutrinos are presented. The contained event analysis of atmospheric neutrinos shows a small value of μ/e ratio and a large asymmetry in the zenith angle distribution. A distortion of zenith angle distribution is observed in the upward-through-going muons resulting from atmospheric neutrino interactions in the rock surrounding the Super–Kamiokande detector. The ratio of upward-stopping muons to upward-through-going muons is significantly smaller than the expectation. All those results on atmospheric neutrinos give evidence for ν_μ oscillations. The obtained neutrino oscillation parameters are Δm^2=$10^{-3} - 10^{-2}\mathrm{eV}^2$ and $\sin^2 2\theta > 0.8$.

Super-Kamiokande observed about 7000 solar neutrino events over 504 days of live time. The observed solar neutrino flux is 47% of the expectation from the standard solar model. No significant day/night difference is observed and a solar model independent limit on neutrino oscillation parameters is obtained. A comparison of the observed recoil electron spectrum with the expectation exhibits a poor agreement at the 4.8% confidence level.

1 Introduction

Atmospheric neutrinos and solar neutrinos are extremely good sources for investigating neutrino oscillations. A probability of neutrino oscillations is given by the following formula:

$$P(\nu_\alpha \to \nu_\beta) = \sin^2 2\theta \sin^2(1.27\frac{L}{E_\nu}\Delta m^2), \quad (1)$$

where θ is the mixing angle of neutrinos, L is the distance from a neutrino source to a detector in units of kilometers, E_ν is the energy of neutrinos in units of GeV, and Δm^2 is the difference of mass squares in units of eV^2. As seen in the equation, one needs longer distances for investigating smaller Δm^2. The neutrino oscillation experiments with a baseline of sun-to-earth and earth-size, namely solar neutrino and atmospheric neutrino experiments, are best suited for searching for small Δm^2.

The atmospheric anomaly was first presented by the Kamiokande[1,2] and IMB[3] experiments. The anomaly suggested neutrino oscillations, but the statistics of those experiments were not enough to give convincing evidence for neutrino oscillations. Super-Kamiokande is almost ten times larger than those experiments and high statistics atmospheric neutrino data have given strong evidence for neutrino oscillations.

The solar neutrino experiments observed significantly lower flux than the expectations from the standard solar models, known as "the solar neutrino problem." One of the possible solutions of the solar neutrino problem is neutrino oscillations. In order to get evidence for neutrino oscillations in solar neutrinos, solar model independent evidence for oscillations should be searched for. Super-Kamiokande tests solar neutrino oscillations using short time variations, such as day/night difference of the flux, and the shape of the energy spectrum.

In this report, results from Super-Kamiokande on atmospheric neutrinos and solar neutrinos are described.

2 Super-Kamiokande Detector

Super-Kamiokande (SK) is a water Cherenkov detector located in the Kamioka Mine in Japan. A schematic view of the detector is shown in Fig. 1.

The water tank consists of inner and outer detectors. The inner detector is composed of 11,146 20-inch diameter photomultiplier tubes (PMTs) placed facing inward on the surface of a 33.8 m diameter by 36.2 m high cylinder. The tubes are spaced on a 0.707 m grid, and enclose 32,000 metric tons of water. The total photocathode surface area of

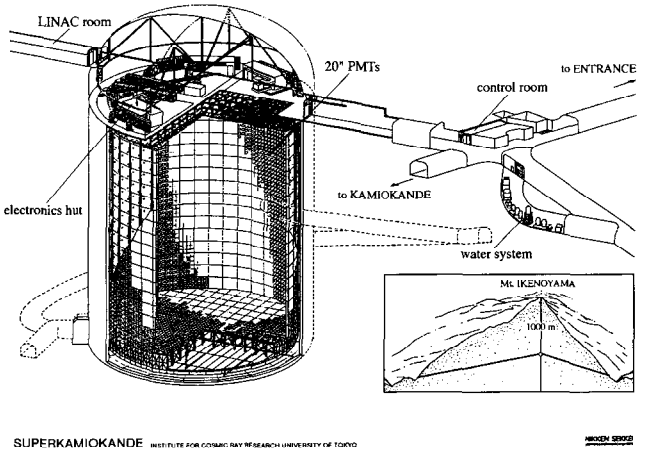

Fig. 1. Schematic view of the Super-Kamiokande detector.

all PMTs is 40% of the surface of the inner detector. A 4π solid-angle outer detector surrounds the inner detector. The outer detector is also a water Cherenkov counter with 1,885 8-inch PMTs facing outwards. The light collection of these smaller PMTs is enhanced by the addition of 60 cm square wavelength shifter plates around each PMT. The thickness of the outer detector is 2.6–2.75 meters. The outer detector is designed to reduce external gamma-rays from surrounding rocks for the solar neutrino analysis and to tag cosmic-ray muons. The fiducial volume of the detector is defined to be more than 2 m inwards from the inner detector phototube wall for the solar neutrino analysis and contained event analysis of atmospheric neutrinos, resulting in a 22-kton fiducial water volume.

A trigger of the detector is issued when more than 29 PMTs give signals within 200 nanoseconds, which corresponds to 5.7 MeV equivalent electron energy. The trigger efficiency for the event above the current analysis threshold of solar neutrinos (6.5 MeV) is better than 99%. The trigger threshold is low enough to observe atmospheric neutrino events.

3 Atmospheric Neutrinos

Atmospheric neutrinos are produced by the interaction of primary cosmic rays in the atmosphere. The hadronic showers resulting from the cosmic ray interaction produces electron and muon neutrinos through $\pi^+ \to \mu^+ + \nu_\mu$ followed by $\mu^+ \to e^+ + \bar{\nu}_\mu + \nu_e$ (and their charge conjugates). The ratio ($\equiv \nu_\mu/\nu_e$) of the flux of $\nu_\mu + \bar{\nu}_\mu$ to the flux of $\nu_e + \bar{\nu}_e$ is expected to be about two from the decay chain of $\pi^\pm$ (it is true for the energy below $\sim$1 GeV). As the energy increases, the ν_μ/ν_e ratio increases, because the fraction of the muons which reach earth's surface increases as their energy. The ν_μ/ν_e ratio is determined by the well-understood decay chain of mesons and the uncertainty of the ratio is less than 5% (Refs. 4 and 5), whereas the absolute flux of each neutrino has an uncertainty of $\sim$25%. Hence, the ν_μ/ν_e ratio is a robust value to test neutrino oscillations. Another way to test neutrino oscillations is the zenith angle of neutrinos. The zenith angle distribution is expected to be up/down symmetric for neutrinos above 1 GeV, where the effects due to the Earth's magnetic field on primary cosmic rays are small. The symmetry is determined by the simple geometry of neutrino production.

The measurements of the ν_μ/ν_e ratio are reported as $R \equiv (\mu/e)_{DATA}/(\mu/e)_{MC}$, where μ and e are the number of muon-like (μ-like) and electron-like (e-like) events observed in the detector for both data and Monte Carlo simulation. This ratio largely cancels experimental and theoretical uncertainties. $R = 1$ is expected if the physics in the Monte Carlo simulation accurately models the data. Measurements of significantly smaller values of R have been reported by Kamiokande,[1,2] IMB,[3] and recently by Super–Kamiokande.[6,7] Although measurements of R by early iron-calorimeter experiments, Fréjus[8] and NUSEX,[9] were consistent with one, the Soudan-2 iron-calorimeter experiment[10] has reported observation of a small value of R.

Super–Kamiokande detects atmospheric neutrinos as (1) contained events, (2) upward-through-going muons, and (3) upward-stopping muons. The contained events are neutrino interactions occuring in the fiducial volume of the inner detector. High energy atmospheric muon neutrinos interact in the rock surrounding Super–Kamiokande produce muons by charged current interactions. They are observed as through-going or stopping muons in the detector. Although the large number of cosmic ray downward going muons limit the observation only to upward-going muons, they cover the angular range from nearly horizontal to vertical directions. The following sub-sections describe results of each analysis.

3.1 Results of Contained Events

The contained events are separated into fully-contained (FC) events and partially-contained (PC) events. The FC events deposit all of their Cherenkov radiation in the inner detector, while PC events have exiting particles which deposit some Cherenkov radiation in the outer detector. For the contained event analysis, the neutrino interaction vertex is required to be reconstructed within the 22.5 kiloton fiducial volume, defined to be > 2 m from the PMT wall. Super–Kamiokande has observed 4353 FC events and 301 PC events in a 33.0 kiloton-year exposure. The FC contained events are divided into sub-GeV ($E_{vis} < 1.33$ GeV) and multi-GeV ($E_{vis} > 1.33$ GeV) samples. The number of Cherenkov rings is counted by an automatic ring counting program and a particle identification program is applied for single ring events. Electrons produce diffused Cherenkov ring patterns whereas muons make clear Cherenkov rings. The diffuseness is evaluated by a likelihood (L) and Fig. 2 shows the L distribution for single ring sub-GeV events. Positive and negative L are defined to be μ-like and e-like, respectively. The figure shows that the μ-like and e-like events are clearly separated and the shape of the L distribution is well reproduced by the Monte Carlo simulation. The particle identification is checked by using muon decay electrons and stopping cosmic ray muons. The misidentification probability is estimated to be 0.6% for sub-GeV events and 2% for multi-GeV events. The particle identification programs have also been tested using beams of electrons and muons incident on a water Cherenkov detector at KEK.[14]

Table 1 summarizes the number of observed events and expectations from the Monte Carlo simulation based on the flux calculation by Honda *et al.*[5] Details of the data analyses of sub-GeV and multi-GeV samples are described in Refs. 6 and 7. The R value for the sub-GeV sample is obtained to be

$$R(sub-GeV) = 0.63 \pm 0.03\,(stat.) \pm 0.05\,(sys.).$$

The PC events are classified as μ-like events, because a Monte Carlo simulation shows that 98% of PC events come from charged current interaction of ν_μ. In the Monte Carlo simulation, 88% (96%) of the sub-GeV e-like (μ-like) events were ν_e (ν_μ) charged-current interactions and 84% (99%) of the multi-GeV e-like (μ-like) events were ν_e (ν_μ) charged-current interactions. The R value for the multi-GeV FC sample and PC sample is obtained to be

$$R(multi-GeV; FC+PC) = 0.65 \pm 0.05\,(stat.) \pm 0.08\,(sys.).$$

The sources of the systematic error of R are uncertainty of the predicted ratio of ν_μ flux

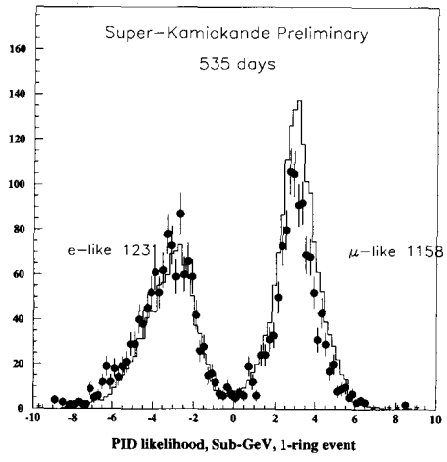

Fig. 2. The particle identification likelihood distribution for single ring sub-GeV events.

	Data	Monte Carlo
sub-GeV		
single-ring	2389	2622.6
e-like	1231	1049.1
μ-like	1158	1573.6
multi-ring	911	980.7
total	3300	3603.3
multi-GeV		
single-ring	520	531.7
e-like	290	236.0
μ-like	230	295.7
multi-ring	533	560.1
total	1053	1091.8
partially-contained	301	371.6

Table 1. Summary of the sub-GeV, multi-GeV, and PC event samples compared with the Monte Carlo prediction based on the neutrino flux calculation by Honda *et al.*[5]

to ν_e flux ($< 5\%$), particle identification efficiency described above, charged-current and neutral current cross sections (3~4%) and ring number counting (3% for sub-GeV and 6% for multi-GeV), etc. The probability that the observed μ/e ratios could be due to statistical fluctuation is less than 0.001% for sub-GeV R and less than 1% for multi-GeV R.

The zenith angle distributions of FC and PC events are shown in Fig. 3 together with the Monte Carlo simulations. The shape of the observed zenith angle distribution

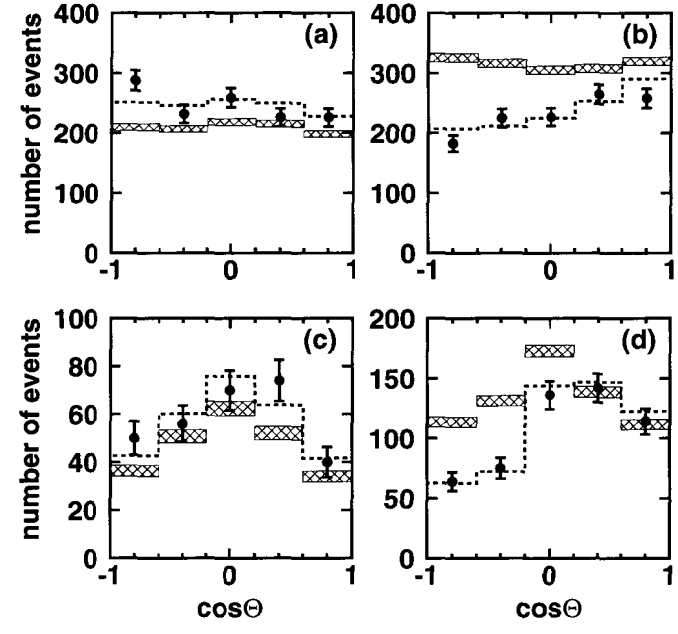

Fig. 3. Zenith angle distribution of atmospheric neutrino events: (a) sub-GeV e-like, (b) sub-GeV μ-like, (c) multi-GeV e-like, and (d) multi-GeV μ-like + PC. The shaded histograms show the expectations from the Monte Carlo simulation and the dotted histograms show the best fit assuming neutrino oscillations (see text).

of e-like events agrees well with the simulation, but the large distortion of the zenith angle distribution is observed in the μ-like events. The shape comparison of the zenith angle distribution between the observed data and Monte Carlo simulation gives a χ^2

of 2.8 with 4 d.o.f. (degrees of freedom) for e-like multi-GeV events, corresponding to 59% of confidence level (CL), and 30 for μ-like multi-GeV events, corresponding to 4.9×10^{-4}% CL. The large χ^2 value in μ-like events comes from the large deficit of upward-going events. Up/down asymmetry is defined as $A = (U-D)/(U+D)$ where U is the number of upward-going events ($-1 < \cos\Theta < -0.2$) and D is the number of downward-going events ($0.2 < \cos\Theta < 1$). The asymmetry is expected to be near zero independent of the flux model for $E_\nu > 1$ GeV as described above. The momentum dependence of the asymmetry is shown in Fig. 4. The asymmetry for e-like events is near

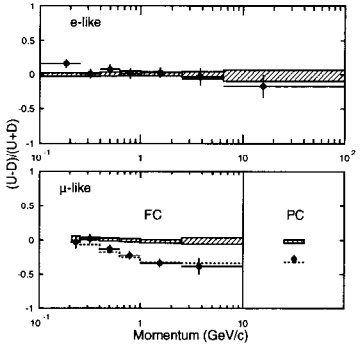

Fig. 4. Momentum dependence of the zenith angle asymmetry of the data (data points) and the Monte Carlo simulation (shaded histograms). The dotted histogram shows the best fit with neutrino oscillations.

zero and consistent with the expectation, while the μ-like events at higher momentum largely deviate from the expectation. The angular correlation between charged leptons and incident neutrinos is estimated by a Monte Carlo simulation and it is 15–20° for multi-GeV events and ~60° for sub-GeV events. Events with $E < 0.4$ GeV essentially do not remember the direction of the incident neutrinos. The main reason why the asymmetry of the μ-like event approaches to zero at lower energy is due to this effect.

We have examined the hypotheses of two-flavor neutrino oscillations of $\nu_\mu \leftrightarrow \nu_e$ and $\nu_\mu \leftrightarrow \nu_\tau$ using a χ^2 comparison of momentum and angular distributions of the data and the Monte Carlo. The contained events are divided into five zenith angle bins and seven momentum bins both for e-like events and μ-like plus PC events (70 bins in total). The χ^2 is defined as

$$\chi^2 = \sum_{cos\Theta,p}^{70} \left(\frac{N_{Data} - N_{MC}(\sin^2 2\theta, \Delta m^2, \epsilon_j)}{\sigma} \right)^2 + \sum_j \left(\frac{\epsilon_j}{\sigma_j} \right)^2 ,$$

where N_{Data} is the measured number of events in each bin. $N_{MC}(\sin^2 2\theta, \Delta m^2, \epsilon_j)$ is the expected number of Monte Carlo events, which is a function of $\sin^2 2\theta$, Δm^2; and ϵ_j, σ_j are parameters which are related to the systematic uncertainties. σ accounts for both data statistics and the weighted Monte Carlo statistics. The parameters for the systematic errors (and their uncertainties) are: E_ν spectral index (0.05), sub-GeV R (8%), multi-GeV R (12%), relative normalization of PC to FC (8%), L/E_ν (15%), up/down ratio for sub-GeV (2.4%), and multi-GeV (2.7%). The absolute normalization of the flux is a free parameter in the analysis. See reference [11] for more details. The best χ^2 is obtained to be 65 for $\nu_\mu \leftrightarrow \nu_\tau$ and 88 for $\nu_\mu \leftrightarrow \nu_e$ oscillations with 67 degrees of freedom. Hence, SK data favors $\nu_\mu \leftrightarrow \nu_\tau$ oscillations more than $\nu_\mu \leftrightarrow \nu_e$ as far as two neutrino oscillations are assumed. The best χ^2 is obtained at $\Delta m^2 = 2.2 \times 10^{-3}$ eV^2 and $\sin^2 2\theta = 1.0$ for $\nu_\mu \leftrightarrow \nu_\tau$ oscillations. The best fit zenith angle distribution is shown by the dotted histogram in Fig. 3.

Neutrino oscillations are a function of L/E_ν as shown in Eq. (1), where L is the neutrino travel path length and E_ν is the primary energy of neutrinos. Super–Kamiokande cannot measure E_ν on an event by event basis, but it can be estimated statistically. The relation between the lepton energy and the neutrino energy was obtained by a Monte Carlo simulation and the L/E_ν distribution is obtained as Fig. 5. The energy of the events is limited to E >0.4 GeV, because events below this energy do not have good resolution in L. The dotted histogram in the figure shows the expectation from the $\nu_\mu \leftrightarrow \nu_\tau$ oscillations with the best fit oscillation parameters. The L/E_ν distributions of e-like and μ-like events agree with the expectation from neutrino oscillations.

An allowed region of neutrino oscillation parameters is obtained as the thick-black curve in Fig. 6 for $\nu_\mu \leftrightarrow \nu_\tau$. The region $\Delta m^2 = 5 \times 10^{-4} - 6 \times 10^{-3}$ eV^2 and $\sin^2 2\theta > 0.83$ is allowed with 90% CL.

The anomalies of the small μ/e double ratio and the distortion of the zenith angle distribution could be due to $\nu_\mu \leftrightarrow \nu_s$ (sterile neutrinos) oscillations. We test $\nu_\mu \leftrightarrow \nu_\tau$ versus $\nu_\mu \leftrightarrow \nu_s$ oscillations using the ratio of the number of π^0 events to e-like events (π^0/e ratio). If the anomalies are due to $\nu_\mu \leftrightarrow \nu_\tau$ oscillations, the π^0 event rate duc

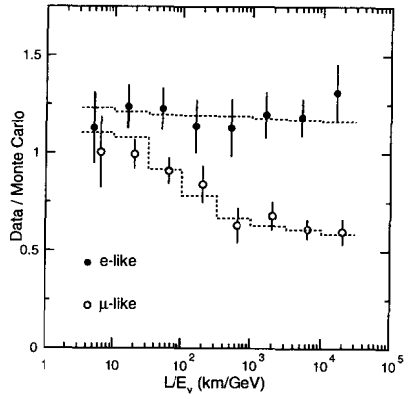

Fig. 5. L/E_ν distributions for e-like and μ-like events. The points show the ratio of observed data to MC expectations without neutrino oscillations. The dotted histogram shows the expected shape for $\nu_\mu \leftrightarrow \nu_\tau$ at $\Delta m^2 = 2.2 \times 10^{-3}\mathrm{eV}^2$ and $\sin^2 2\theta = 1$.

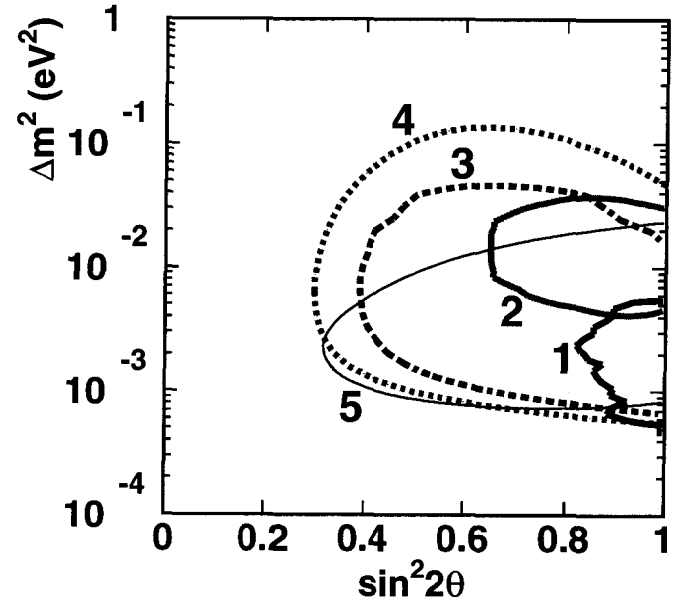

Fig. 6. Allowed regions of neutrino oscillation parameters obtained by the analyses of contained events [thick-black (1)], upward-through-going muons [thick-dotted (3)] and upward *stop/through* muons ratio [thin-solid (5)]. Also shown are results from Kamiokande contained event analysis [thick-gray (2)] and upward-through-going muons [thick-gray-dotted (4)].

to neutral current interactions does not change and the π^0/e ratio is the same as the expectation without neutrino oscillations. On the other hand, if it is due to $\nu_\mu \leftrightarrow \nu_s$ oscillations, the π^0/e ratio should be smaller than the expectation, because ν_s does not cause a neutral current interaction. The π^0/e ratio is expected to be $\sim$83% of the no-mixing expectation, for $\nu_\mu \leftrightarrow \nu_s$ with the oscillation parameters obtained above. Figure 7 shows invariant mass distribution for two e-like ring events. A clear signature of π^0 events are seen around the π^0 mass. The events in the mass range of 90–190 MeV/c^2 are selected as π^0 candidates.

The comparison of the π^0/e ratio of data and Monte Carlo gives

$$\frac{(\pi_0/e)_{data}}{(\pi_0/e)_{MC}} = \frac{210/1231}{192.5/1049.1} = 0.93 \pm 0.07\,(stat.) \pm 0.19\,(sys.).$$

The π^0/e double ratio is consistent with $\nu_\mu \leftrightarrow \nu_\tau$. But, because of the current large

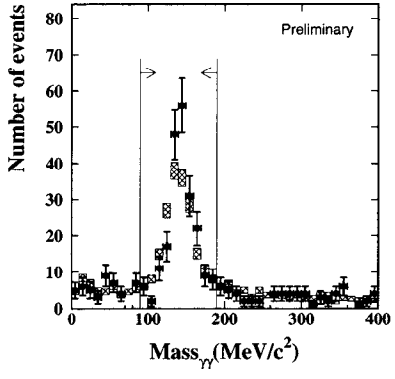

Fig. 7. Invariant mass distribution of two e-like ring events. The shaded histogram shows the Monte Carlo simulation and the vertical spread of the histogram shows the statistical error of the Monte Carlo simulation. The cut region for π^0 events is also shown.

systematic error, we cannot differentiate $\nu_\mu \leftrightarrow \nu_\tau$ and $\nu_\mu \leftrightarrow \nu_s$ at present. The main source of the systematic error is the uncertainty of the cross section of the neutral current π^0 production. Fortunately, we will start the K2K long baseline experiment next year. We will construct a one kilo-ton water Cherenkov (1kt) detector at KEK. The 1kt detector is able to measure the cross section quite precisely. Hence, in the near future we can discuss the π^0/e double ratio with a much smaller systematic error.

3.2 Upward-Going Muons

Atmospheric muon neutrinos which interact in the rock surrounding the SK tank produce muons by charged current interactions and the resulting muons pass through the SK detector. Although downward-going muons are dominated by cosmic-rays, upward-going muons are pure samples of atmospheric neutrinos. We analyze two types of upward-going muons. One is upward-through-going muons, which have signals of muon entrance and exit in the outer detector and pass through the inner detector. The path length of the through-going muons is required to be longer than seven meters in this analysis. The other type is upward-stopping muons, which is the same as upward-through-going muons but they have only entrance signals in the outer detector. Figure 8 shows calculated energy distributions of primary atmospheric neutrinos which cause upward-through-going or upward-stopping muons. The averaged neutrino energy is $\sim$100 GeV for upward-through-going muons and $\sim$10 GeV for upward-stopping muons. We expect a large reduction of flux for near vertical upward-through-going muons and small reduction for near horizontal direction with the oscillation parameters given by the contained event analysis. On the other hand, the flux of upward-stopping muons must be reduced for the entire zenith angle range by neutrino oscillations.

Super-Kamiokande observed 617 upward-through-going muons for 534 days of live time. The observed flux of atmospheric neutrinos is 1.75$\pm$0.07(stat.)$\pm$0.09(sys.) ($\times 10^{-13}/cm^2/sec/str$). On the other hand, the expected flux is 1.88 $\pm$ 0.4 ($\times 10^{-13}$ $/cm^2/sec/str$) using the flux calculation by Honda *et al.*[5] and 2.02 $\pm$ 0.4 ($\times 10^{-13}$ $/cm^2/sec/str$) using Bartol flux.[4] Neutrino interactions are simulated by using the structure function of GRV94DIS[12] and the energy loss of muons is based on the calculation by Lohmann *et al.*[13] Because of the $\sim$20% error in expected flux calculation, we use only the shape of the zenith angle distribution for the neutrino oscillation analysis for upward-through-going muons. The zenith angle distribution of the flux is shown in Fig. 9 together with the expectation using the Honda flux. The observed flux in the near horizontal direction agrees with the expectation, but most of the data points near the vertical direction are lower than the expectation. The shape comparison between the data and the expectation gives a χ^2 of 18.3 with 9 d.o.f., corresponding to 3.2% CL. By assuming the neutrino oscillations, the best fit of the shape of the zenith angle

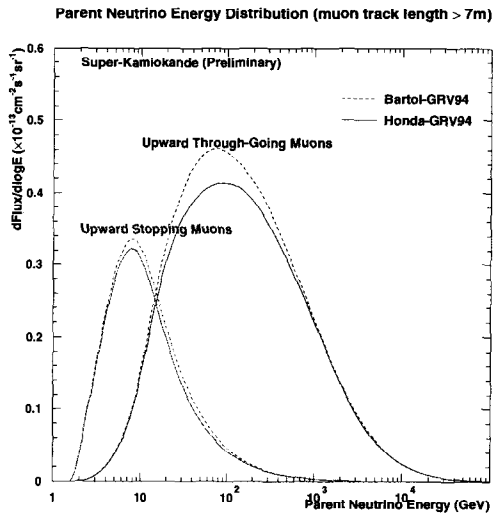

Fig. 8. Calculated primary neutrino energy distributions for upward-through-going and upward-stopping muons. The solid and dotted curves are based on the flux calculations by Bartol[4] and Honda *et al.*,[5] respectively.

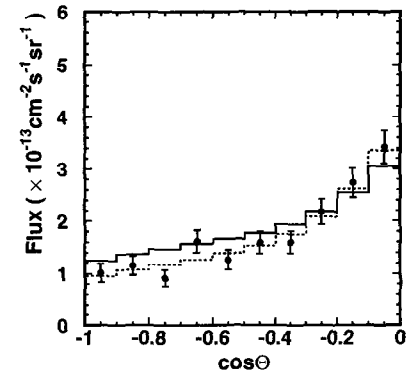

Fig. 9. Zenith angle distribution of the flux of upward-through going muons. Solid histograms show Monte Carlo expectations without neutrino oscillations. The dotted histogram shows the best fit with neutrino oscillations.

distribution is obtained at $\Delta m^2 = 2.5 \times 10^{-3}$ eV^2 and $\sin^2 2\theta = 1.0$. The χ^2 for the fit is 7.3 with 9 d.o.f. (61% CL). The absolute normalization of the flux is a free parameter in the fit. The best fit zenith angle distribution is shown by a dotted histogram in Fig. 9. An allowed region of the neutrino oscillation parameters is shown by the thick-dotted curve in Fig. 6 and the region overlaps with the one obtained by contained event analysis quite well.

The neutrino oscillation parameters obtained by the contained events analysis suggest that neutrinos with $E_\nu \lesssim 40$ GeV should be largely oscillated in traveling the distance of earth's diameter, whereas neutrinos with $E_\nu \gg 40$ GeV do not oscillate so much. Hence, the oscillation effect is larger for upward-stopping muons than the upward-through-going muons as seen in Fig. 8. Super–Kamiokande has observed 137 upward-stopping muons during 516 days' live time. We use the ratio of the numbers of stopping muons to through-going muons ($stop/through$ ratio) for the test of neutrino oscillations, because it cancels the absolute normalization of the flux. The $stop/through$ ratio is compared between data and a Monte Carlo simulation and:

$$\frac{(stop/through)_{data}}{(stop/through)_{MC}} = \frac{0.22 \pm 0.023 \pm 0.014}{0.39 \pm 0.05} = 0.56 \pm 0.10.$$

The value is significantly smaller than unity. Figure 10 shows the zenith angle distribu-

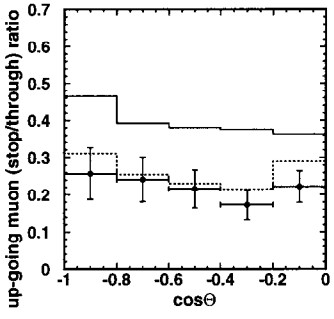

Fig. 10. Zenith angle distribution of the *stop/through* ratio of the upward going muons. The solid histogram shows the expected ratio without neutrino oscillations. The dashed histogram shows the expectation for $\nu_\mu \leftrightarrow \nu_\tau$ oscillations with $\sin^2 2\theta = 1.0$ and $\Delta m^2 = 3 \times 10^{-3}$ eV^2. The expected *stop/through* ratio has $\pm 14\%$ uncertainty.

tion of the *stop/through* ratio together with the predictions with and without neutrino oscillations. The prediction with neutrino oscillations agrees well with the data within the systematic uncertainty ($\pm 14\%$). The allowed region of neutrino oscillation parameters obtained by the *stop/through* ratio is shown by the thin-solid curve in Fig. 6. The allowed region overlaps with the one obtained by the contained event analysis.

3.3 Summary

The small μ/e ratio and the distortion of the zenith angle distribution in contained events give evidence for ν_μ oscillations. The analyses of the zenith angle dependence of upward-through-going muons and the *stop/through* ratio confirm the results obtained by the contained event analysis. The obtained neutrino oscillation parameters are Δm^2 of $10^{-3} - 10^{-2}$eV^2 and $\sin^2 2\theta > 0.8$.

4 Solar Neutrinos

Solar neutrinos had been observed by the Homestake experiment,[15] Kamiokande,[16] GALLEX,[17] and SAGE.[18] All these experiments observed significantly smaller solar neutrino flux than the expectations from standard solar models (SSMs),[19–21] known as "the solar neutrino problem." It is suggested that explaining the results of all four experiments in the framework of SSM has a difficulty, even if the input parameters of the SSM are changed. One possible way to explain all these results is neutrino oscillations.[22] Analysis taking into account the MSW mechanism of neutrino oscillations suggests neutrino oscillation parameters around $\Delta m^2 \sim 6 \times 10^{-6}$ eV^2 and $\sin^2 2\theta \sim 5 \times 10^{-3}$ (small mixing angle solution), $\Delta m^2 \sim 10^{-5} - 10^{-4}$ eV^2 and $\sin^2 2\theta \sim 0.6$ (large mixing angle solution), and $\Delta m^2 \sim 10^{-11}$ eV^2 and $\sin^2 2\theta \sim 1$ (just-so solution).[23,24] In order to test neutrino oscillations without relying on solar models, quantities which are independent from SSM expectations should be used. Short time variations of the solar neutrino flux, such as the day/night difference of the flux, could be observed in case of a large mixing angle solution and a part of a small mixing angle solution. And a distortion of the neutrino energy spectrum could be observed in case of small mixing angle and just-so solutions. Super-Kamiokande is a real-time detector and measures ^{8}B solar neutrinos by neutrino-electron scattering. Super-Kamiokande is able to measure precise neutrino flux variation and spectrum of solar neutrinos.

4.1 Calibration

The calibration of the detector is quite important for the solar neutrino measurement. Especially, absolute energy calibration is essential for the spectrum measurement. In order to perform precise calibration of absolute energy scale, energy resolution, and angular resolution, an electron linear accelerator (LINAC) was constructed near the SK tank.[25] An electron beam from the LINAC is transported into the SK tank. The LINAC injects monoenergetic electrons with a tunable energy ranging from 5 to 16 MeV. The absolute energy of the beam is measured by a germanium detector, which was in turn calibrated by gamma-ray sources and internal-conversion electrons from a ^{207}Bi source. The uncertainty of the beam energy is less than 20 keV over the energy range covered by the LINAC. LINAC data were taken at eight representative positions in the Super–Kamiokande inner volume with seven different momenta ranging from 4.89 to 16.09 MeV. Figure 11 shows energy distributions of the LINAC data taken at a

typical position overlaid with corresponding Monte Carlo (MC) simulations.

The LINAC data and MC distributions agree with each other quite well. The peak

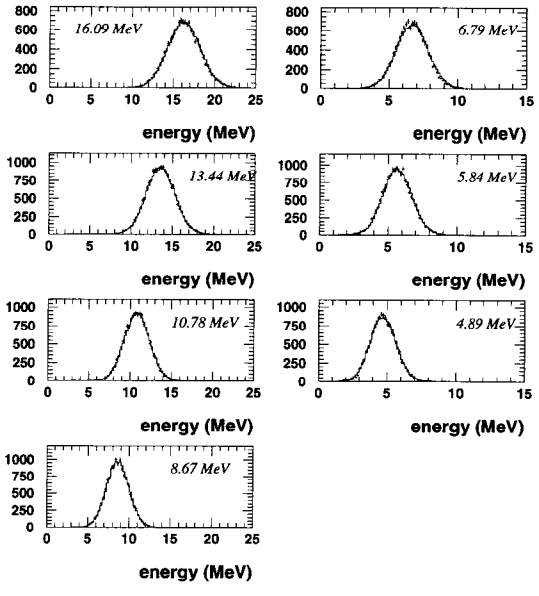

Fig. 11. LINAC (crosses) and MC (histogram) energy distributions for LINAC calibration data.

position of the distributions indicates the absolute energy scale. Figure 12 shows the absolute energy scale difference between data and MC simulation. The detector position dependence of the energy scale is estimated to be 0.5% in rms using the LINAC calibration. The uncertainty of the absolute energy in the LINAC calibration system itself is 0.55% at 6 MeV and 0.3% at 10 MeV. The LINAC calibration data was taken only in the downward-going direction at the moment. The energy scale for all directions are checked using beta-rays from spallation products induced by cosmic-ray muons and the directional dependence of the absolute energy scale is measured to be less than 0.5%. Adding all possible sources of uncertainties, the absolute energy scale is calibrated with

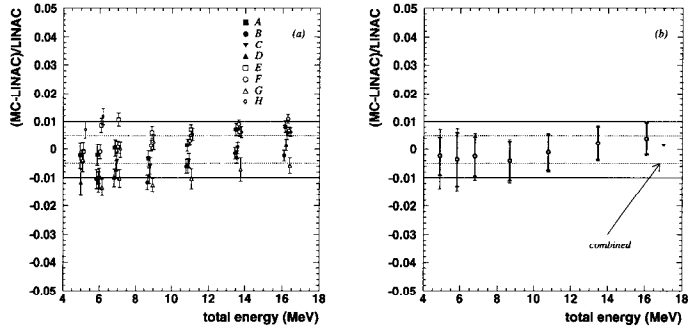

Fig. 12. Comparison of absolute energy scales for LINAC and MC. (a) the difference of the absolute energy scale for each LINAC position; (b) position average. The last point in (b) represents the total average over all positions and beam energies.

an accuracy of 0.8% at 10 MeV.

The energy resolution is also calibrated using the LINAC. The observed energy resolution is, for example, 1.58 MeV for 10.78 MeV electrons, and the measured energy resolution agrees with the MC simulation better than 2%. Angular resolution is also calibrated by the LINAC. Figure 13 shows the opening angle between the reconstructed electron direction and the direction of beam injection for MC and LINAC at a typical position. The measured angular resolution is 2–3% smaller than the one obtained by the current MC simulation. The difference is corrected in extracting solar neutrino flux from the observed data.

The stability of the detector is monitored by using decay electrons from stopping cosmic-ray muons and beta-decay nuclei from spallation products. The time variation of the water transparency is monitored by using the decay electrons and the obtained water transparency is used to calculate energy for each event. Applying the water transparency correction, the stability of the energy scale is better than $\pm 0.5\%$ for over two years. The absolute energy calibration is cross-checked by using the decays of ^{16}N produced by stopping muon capture on oxygen. The difference in energy scales between that obtained by ^{16}N decay beta spectrum and the MC tuned by LINAC is $0.2\ ^{+0.6}_{-0.8}\%$.

In summary, the energy response and angular response of the SK detector are cali-

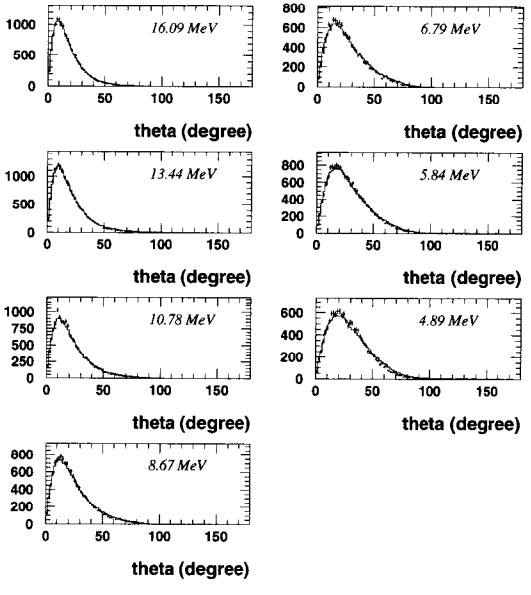

Fig. 13. Angular distributions for a typical LINAC calibration data. The histogram is MC, points LINAC.

brated quite precisely and they are enough for testing flux time variations and the energy spectrum of solar neutrinos at the present statistical level.

4.2 Data Analysis

SK has obtained 504 live days' data between 31 May 1996 and 25 March 1998. The obtained data were reduced by applying the following cuts[26]: (1) less than 20 hits in the outer detector (i.e., select contained events), (2) less than 1000 photoelectrons, corresponds to 110∼120 MeV, and (3) time to the previous event is more than 20 μs (to reject decay electrons from stopping cosmic-ray muons). The event rate after the reduction is ∼57 events/day/kton above 6.5 MeV. The efficiency of the reduction for solar neutrino signals is 94.2%. The main source of the background after the reduction is muon–induced spallation products. They are rejected by using the time from the preceding muon, distance between the vertex of low energy event and the muon track, and pulse height of the muon. The spallation cut reduces the event rate to ∼12 events/day/kton. The dead time induced by this cut is 20.0%, which gives maximum significance, defined to be solar neutrino signal/$\sqrt{\text{background}}$. The data was finally reduced by removing the gamma-ray background coming from the wall of the detector by requiring more than 4.5 m in the length of the backward extrapolated vector from the event vertex to the inner detector wall. This cut gives a final event rate of ∼7.6 events/day/kton with an estimated loss of 7.8% of solar neutrino signal.

Figure 14 shows the angular distribution of the final events with respect to the direction of the sun. A clear enhancement of solar neutrino signal is seen in the direction of the sun. The solar neutrino signal amounts to $6820^{+150}_{-130}(stat.)$ events for the 504 days' data. Using the expected energy shape of ^{8}B solar neutrinos, the flux of ^{8}B solar neutrinos is obtained to be $[2.44\pm0.05(stat.)^{+0.09}_{-0.07}(syst.)] \times 10^6/\text{cm}^2/\text{s}$. Major sources of the systematic error in the flux are (1) uncertainty in absolute energy scale and resolution ($^{+2.2}_{-2.1}$% error in flux), (2) uncertainty in angular resolution (+2.2%), (3) uncertainty in the ^{8}B spectral shape ($^{+2.2}_{-2.1}$%). Comparing the obtained flux with the SSM predictions, the ratio of flux between the SK data and SSM prediction (data/SSM) is $0.474^{+0.010}_{-0.009}(stat.)^{+0.017}_{-0.014}(syst.)$ using the latest SSM by Bahcall *et al.*[19] The obtained ratio is significantly smaller than unity. The time variation of solar neutrino flux is shown in Fig. 15. The curve in the figure shows expected flux variation due to the eccentricity of the earth. The absolute flux of the expectation is reduced to 47%. Comparing the observed time variation of the flux with the expectation, χ^2 is 8.78 with 14 degrees of

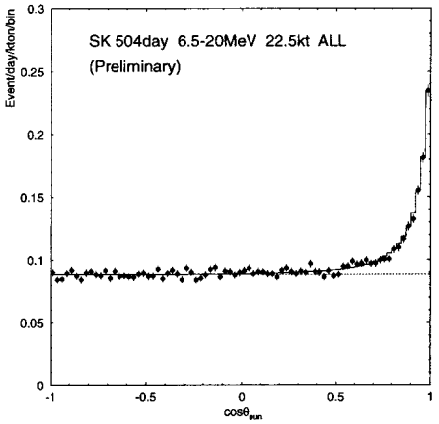

Fig. 14. Angular distribution of the final events with respect to the direction of the sun.

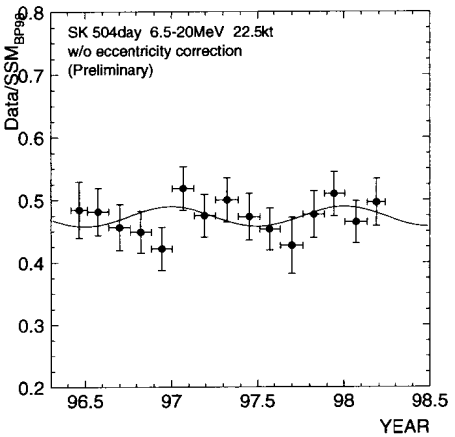

Fig. 15. Time variation of the solar neutrino flux. The curve in the figure shows expected flux variation due to the eccentricity of the earth.

freedom (d.o.f.), which corresponds to 84.4% CL. Hence, no significant time variation of the flux over the expected variation is observed.

4.3 Day/Night Analysis

The obtained data was divided into day and night samples, where day and night are defined to be whether the sun is above or below horizon. The observed solar neutrino flux is $[2.37\pm0.07(stat.)^{+0.08}_{-0.07}(syst.)] \times 10^6/\mathrm{cm}^2/\mathrm{s}$ for day-time and $[2.48^{+0.07}_{-0.06}(stat.)^{+0.09}_{-0.07}(syst.)] \times 10^6/\mathrm{cm}^2/\mathrm{s}$ for night-time. The difference of the flux between day-time(D) and night-time(N) is given as

$$\frac{D-N}{D+N} = -0.023 \pm 0.020 \pm 0.014.$$

Thus, there is no significant day/night difference. The night-time data was subdivided into five bins according to the zenith angle of the sun (θ_z) at the time when the neutrino event is observed, N1 ($0 < \cos(\theta_z) \leq 0.2$), N2 ($0.2 < \cos(\theta_z) \leq 0.4$), ..., N5 ($0.8 < \cos(\theta_z) \leq 1.0$). Neutrinos pass through the mantle for N1 to N4 and through the core of the earth in the case of N5. The flux of each data set is shown in Fig. 16. The χ^2 for the night 5 bins assuming a flat distribution is 5.87 with 4 d.o.f. (20.9 % CL). Therefore, no significant variation of the flux during the night-time is observed.

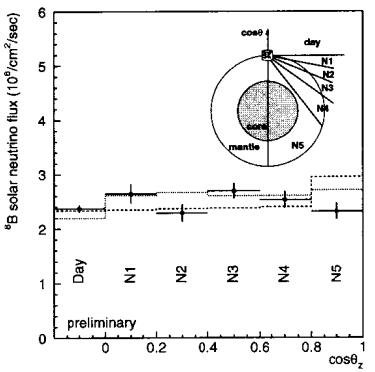

Fig. 16. Flux of solar neutrinos for day-time and night-time samples. The histograms are expectations from neutrino oscillations (see text).

Using the day/night comparison, a solar model independent constraint on neutrino oscillation parameters is obtained. The dotted and dashed histograms in Fig. 16 show expected flux variations for the examples of the large mixing angle solution ($\sin^2 2\theta$ = 0.56, $\Delta m^2 = 1.2\times10^{-5}$ eV^2) and the small mixing angle solution ($\sin^2 2\theta = 0.01$, Δm^2 = 6.3×10^{-6} eV^2) assuming $\nu_e \rightarrow \nu_\mu(\nu_\tau)$ oscillations. Large variation of the flux during night-time is expected for the large mixing angle solution and increase of flux in N5 is expected for the small mixing angle solution. A flux independent constraint on neutrino oscillation parameters is given by using the following χ^2:

$$\chi^2 = \sum_{i=D,N1,\cdots,N5} \left\{ \frac{\phi_i - \alpha \times \phi_{SSM} \times R_i(\sin^2 2\theta, \Delta m^2)}{\sigma_i} \right\}^2,$$

where ϕ_i is the observed flux, ϕ_{SSM} is the flux expected from the SSM, $R_i(\sin^2 2\theta, \Delta m^2)$ is the ratio of the event rate with and without neutrino oscillations, σ_i is the error of observed flux (statistical errors and systematic errors are added quadratically), and α is a normalization factor of the solar neutrino flux. α is a free parameter in the χ^2. The region where $\chi^2 > 15.09$ is excluded with 99% CL as shown in Fig. 17. As a reference, the shaded regions show allowed regions of oscillation parameters which were obtained by comparing the observed flux by Homestake, GALLEX, SAGE, and SK with the corresponding expectations from SSM.[19] A bottom part of the large mixing angle solution and a small part of the small mixing angle solution are excluded by the model independent analysis using day/night flux variation.

4.4 Energy Spectrum Analysis

The obtained final data sample is sub-divided into 16 energy bins, every 0.5 MeV from 6.5 to 14.0 MeV and one bin combining energies from 14.0 to 20.0 MeV. The number of solar neutrino events in each energy bin is extracted from the data by fitting each angular distribution to the sun with a background angular distribution and the expected angular distribution of solar neutrino signals. The background angular distribution is obtained by mapping the remaining background to the direction of the sun. The uncertainty of the flux due to the background angular distribution is estimated to be 0.1%. The number of solar neutrino events thus obtained is shown in Fig. 18. The histogram in the figure shows the expected spectrum from the SSM, which was calculated using the total ^{8}B solar neutrino flux from Ref. 19 (BP98) (5.15×10^6/cm^2/s), the calculation of ^{8}B neutrino spectral shape from Ref. 27, and the electron spectrum of ν-e scattering from Ref. 28, in which radiative corrections are taken into account. The response of the

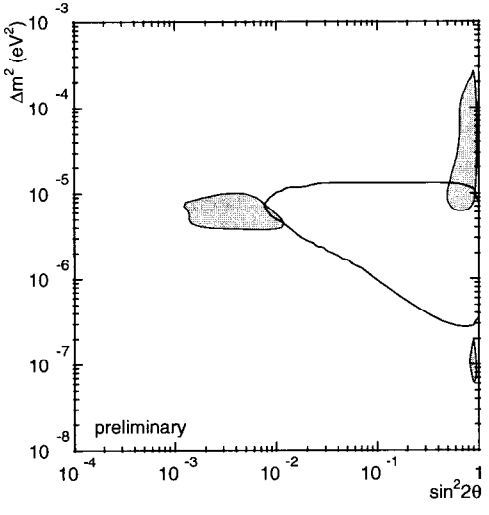

Fig. 17. Excluded region of neutrino oscillation parameters using the model independent day/night analysis with 99% CL for $\nu_e \rightarrow \nu_\mu(\nu_\tau)$ oscillations (white region). The shaded regions show allowed regions of oscillation parameters obtained by using the measured flux of solar neutrino experiments (see text).

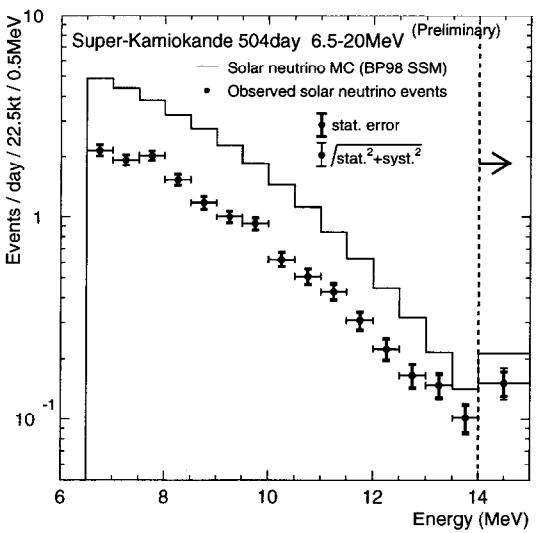

Fig. 18. Energy spectrum of recoil electrons. The inner error shows statistical error and outer error shows systematic error. The histogram shows the expected energy spectrum (see text).

detector, such as the smearing of the electron energy spectrum by the detector energy resolution, is also taken into account by a full MC simulation. In order to compare the shape of the observed energy spectrum with the expected spectrum, the ratio of the spectra are taken as shown in Fig. 19. Systematic errors in the energy shape comparison

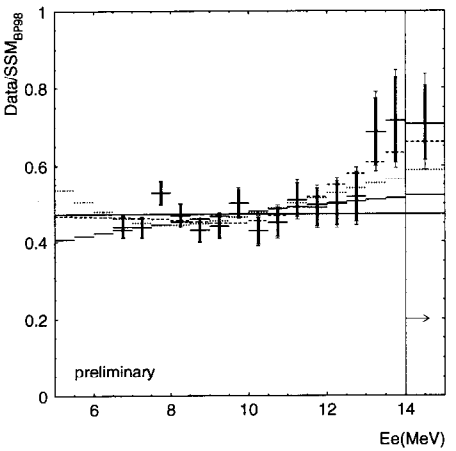

Fig. 19. Ratio of observed energy spectrum to expected spectrum. Inner and outer error bars show statistical and systematic errors, respectively. The dashed histogram shows the best fit assuming neutrino oscillations obtained with $\sin^2 2\theta = 0.93$, $\Delta m^2 = 4.2\times10^{-10}$ eV^2. The solid and dotted histograms show a typical small mixing angle solution ($\sin^2 2\theta = 5\times10^{-3}$, $\Delta m^2 = 7.1\times10^{-6}$ eV^2) and a just-so solution ($\sin^2 2\theta = 0.83$, $\Delta m^2 = 7.1\times10^{-11}$ eV^2), respectively. $\nu_e \rightarrow \nu_\mu(\nu_\tau)$ oscillations are assumed here.

are classified into energy-bin-correlated (called "correlated" from now on) errors and energy-bin-uncorrelated ("uncorrelated") errors. The sources of correlated errors are uncertainties in the absolute energy scale and energy resolution, and uncertainty in the expected energy shape of neutrinos from ^{8}B decays. For example, the correlated errors for the 13.0 to 13.5 MeV energy bin is $^{+6.9}_{6.2}$% from the uncertainties of energy scale and resolution, and $^{+4.7}_{-3.8}$% from the uncertainty of the expected energy shape. The sources of uncorrelated errors are uncertainties in trigger efficiency, data reduction efficiency,

angular resolution, etc. The sum of uncorrelated errors is estimated to be $^{+2.1}_{-1.7}$% for the 6.5 to 7.0 MeV energy bin and ± 1.7% for other energy bins. The sum of correlated and uncorrelated systematic errors is shown as outer error bars in Fig. 19. The statistical significance of the possible distortion of the energy spectrum is discussed using the following χ^2:

$$\chi^2 = \sum_{i=1}^{16} \left\{ \frac{(\frac{data}{SSM})_i - \alpha/(1+\delta_{i,corr} \times \beta)}{\sigma_i} \right\}^2 + \beta^2,$$

where $\delta_{i,corr}$ is the 1σ error of the correlated error described above, σ_i is an 1σ error for each energy bin defined as a sum of the statistical error and uncorrelated errors added quadratically, and α is a free parameter which indicates the relative flux of ^{8}B solar neutrinos. β is a free parameter to constrain the magnitude of the correlated error. The minimum χ^2 is obtained to be 25.1 with 15 d.o.f., which corresponds to 4.8% CL.

The possible contribution of high energy solar neutrinos from $^3He + p \rightarrow {}^4\mathrm{He} + e^+ + \nu_e$ (hep) is estimated using the best estimate flux in BP98, $2.1 \times 10^3/\mathrm{cm}^2/\mathrm{s}$. The expected number of hep events during the 504 days' period is 2.1 for energy above 13.0 MeV, corresponding to 1.0% of the observed solar neutrino events. The error of the expected hep neutrino flux is not precisely estimated in BP98, but unless the expectation is drastically wrong, the contribution of the hep neutrino is negligible at the present statistical level.

Preliminary neutrino oscillation analysis is performed using the spectral shape together with the day/night difference. χ^2 for the oscillation analysis is defined to be

$$\chi^2 = \sum_{D,N} \sum_{i=1}^{i=16} \left\{ \frac{(\frac{data}{SSM})_i - \alpha \times R_i(sin^2 2\theta, \Delta m^2)/(1+\delta_{i,corr} \times \beta)}{\sigma_i} \right\}^2 + \beta^2,$$

where $R_i(sin^2 2\theta, \Delta m^2)$ is the ratio of electron energy spectrum with and without neutrino oscillations. $\nu_e \rightarrow \nu_\mu(\nu_\tau)$ oscillations are assumed here. The minimum χ^2 is obtained to be 38.7 with 31 d.o.f. (16.1 % CL) at $\sin^2 2\theta = 0.93$, $\Delta m^2 = 4.2 \times 10^{-10}$ eV^2. The best fit energy spectrum is shown by the dotted histogram in Fig. 19. The χ^2 calculated by combining day and night spectra is 13.2 with 15 d.o.f. (58% CL). Typical small mixing angle and just-so solutions are also shown in Fig. 19, and χ^2 (day/night combined) for them are 23.0 (8.5% CL) and 18.9 (22% CL), respectively. Allowed regions of neutrino oscillation parameters are obtained as Fig. 20 with 99% CL. The current analysis on the solar neutrino spectrum is not able to give a definite statement on neutrino oscillations, because the current statistical significance is not high enough

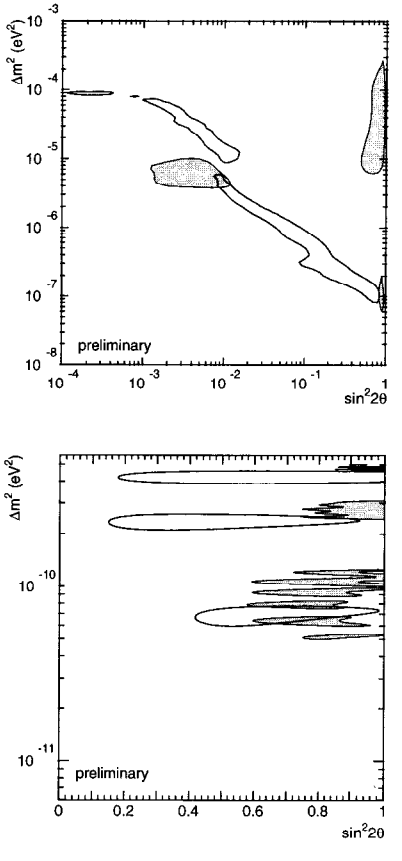

Fig. 20. White regions show allowed regions of neutrino oscillation parameters obtained by using the spectral shape analysis with 99% CL. The shaded regions show the allowed region obtained by the flux comparison between solar neutrino experiments and SSM predictions. $\nu_e \rightarrow \nu_\mu(\nu_\tau)$ oscillations are assumed.

to discuss possible solutions. But, in the future, increasing statistics and lowering the analysis energy threshold should enable us to pinpoint neutrino oscillations using the shape of the energy spectrum. In fact, the spectrum below 6.5 MeV should differentiate possible parameters of neutrino oscillations as seen in Fig. 19.

5 Conclusions

Results of atmospheric neutrinos observed by contained events, upward-through-going muons, and upward-stopping muons are presented. The small μ/e ratio is observed in the contained events and large zenith angle asymmetry is observed in μ-like events. Those anomalies can be explained consistently by neutrino oscillations. The zenith angle distortion of upward-through-going muons and the small $stop/through$ ratio of upward-going muons confirm the results of the contained event analyses. The allowed region of neutrino oscillation parameters obtained by the three independent analyses overlap quite well and the obtained neutrino oscillation parameters are Δm^2 of $10^{-3} - 10^{-2}\mathrm{eV}^2$ and $\sin^2 2\theta > 0.8$.

Preliminary results from 504 days' solar neutrino data of Super-Kamiokande is presented. The observed flux of ^{8}B solar neutrinos is $[2.44\pm0.05(\mathrm{stat.})^{+0.09}_{-0.07}(\mathrm{syst.})] \times 10^6/\mathrm{cm}^2/\mathrm{s}$, which corresponds to 47% of the value expected from the standard solar model.[19] Analysis of the day/night difference and the flux variation during the night-time does not show significant flux variations. This result gives a model independent excluded region on neutrino oscillation parameters as shown in Fig. 17. The spectral shape comparison between the observation and the expectation gives a χ^2 of 25.1 (corresponding to 4.8%) with 15 d.o.f. above 6.5 MeV. A future increase of statistics and lowering the analysis energy threshold should provide fruitful information on neutrino oscillations.

References

[1] K. S. Hirata *et al.*, Phys. Lett. B **205**, 416 (1988); K. S. Hirata *et al.*, Phys. Lett. B **280**, 146 (1992).

[2] Y. Fukuda *et al.*, Phys. Lett. B **335**, 237 (1994).

[3] D. Casper *et al.*, Phys. Rev. Lett. **66**, 2561 (1991); R. Becker-Szendy *et al.*, Phys. Rev. D **46**, 3720 (1992).

[4] G. Barr *et al.*, Phys. Rev. D **39**, 3532 (1989); V. Agrawal *et al.*, Phys. Rev. D53, 1313 (1996); T. K. Gaisser and T. Stanev, Proc. 24th Int. Cosmic Ray Conf. (Rome) Vol. 1, 694 (1995).

[5] M. Honda *et al.*, Phys. Lett. B **248**, 193 (1990); M. Honda *et al.*, Phys. Rev. D **52**, 4985 (1995).

[6] Y. Fukuda, *et al.*, Phys. Lett. B **433**, 9 (1998).

[7] Super-Kamiokande Collaboration, Y. Fukuda *et al.*, Phys. Lett. B **436**, 33 (1998).

[8] K. Daum *et al.*, Z. Phys. C **66**, 417 (1995).

[9] M. Aglietta *et al.*, Europhys. Lett. **8**, 611 (1989).

[10] W. W. M. Allison *et al.*, Phys. Lett. B **391**, 491 (1997); T. Kafka, Proceedings of 5th Int. Workshop on Topics in Astroparticle and Underground Physics, Gran Sasso, Italy, Sept. 1997.

[11] Y. Fukuda *et al.*, Phys. Rev. Lett. **81** (1998) 1562.

[12] M. Glück, E. Reya, and A. Vogt, Z. Phys. C **67**, 433 (1995).

[13] W. Lohmann, R. Kopp, and R. Voss, CERN Yellow Report No. 85-03.

[14] S. Kasuga *et al.*, Phys. Lett. B **374**, 238 (1996).

[15] R. Davis, Prog. Part. Nucl. Phys. **32**, 13 (1994); B. T. Cleveland *et al.*, Nucl. Phys. B (Proc. Suppl.) **38**, 47 (1995).

[16] K. S. Hirata *et al.*, Phys. Rev. Lett. **65**, 1297 (1990); K. S. Hirata *et al.*, Phys. Rev. D **44**, 2241 (1991); D **45**, 2170E (1992); Y. Fukuda *et al.*, Phys. Rev. Lett. **77**, 1683 (1996).

[17] P. Anselmann *et al.*, Phys. Lett. B **327**, 377 (1994): B*342*, 440 (1995).

[18] J. N. Abdurashitov *et al.*, Phys. Lett. B **328**, 234 (1994).

[19] J. N. Bahcall, S. Basu, and M. Pinsonneault, Phys. Lett. B **433**, 1 (1988).

[20] J. N. Bahcall and M. Pinsonneault, Rev. Mod. Phys. **67**, 781 (1995).

[21] S. Turck-Chieze and I. Lopes, Ap. J. **408**, 347 (1993).

[22] S. P. Mikheyev and A. Y. Smirnov, Sov. Jour. Nucl. Phys. **42**, 913 (1985); L. Wolfenstein, Phys. Rev. D **17**, 2369 (1978).

[23] N. Hata and P. Langacker, Phys. Rev. D **56**, 6107 (1997).

[24] P. Langacker, talk presented in NEUTRINO '98, Proceedings of the XVIII International Conference on Neutrino Physics and Astrophysics, Takayama, Japan, 4-9 June 1998, edited by Y. Suzuki and Y. Totsuka, Nucl. Phys. B (Proc. Suppl.) **77**, 241 (1999).

[25] M. Nakahata *et al.*, Nucl. Instrum. Meth. A **421**, 113 (1999).

[26] Y. Fukuda *et al.*, Phys. Rev. Lett. **81**, 1158 (1998).

[27] J. N. Bahcall *et al.*, Phys. Rev. C **54**, 411 (1996).

[28] J. N. Bahcall *et al.*, Phys. Rev. D **51**, 6146 (1995).